Oxidation resistance of quintuple Ti-Al-Si-C-N coatings and associated mechanism

Guizhi Wu, Shengli Ma,[a] and Kewei Xu
State Key Laboratory for Mechanical Behavior of Materials, Xi'an Jiaotong University, Xi'an 710049, China

Vincent Ji
ICMMO/LEMHE, Universite Paris-Sud 11, 91405 Orsay Cedex, France

Paul K. Chu
Department of Physics and Materials Science, City University of Hong Kong, 83 Tat Chee Avenue, Kowloon, Hong Kong, China

(Received 15 September 2011; accepted 8 May 2012; published 23 May 2012)

The oxidation behavior of Ti-Al-Si-C-N hard coatings with different Al contents deposited on high-speed steel and Si substrates by hybrid arc-enhanced magnetron sputtering is investigated in the temperature range of 500 °C–1000 °C. The coating hardness is maintained at around 35 GPa, and the parabolic oxidation rate constant K_p at 1000 °C decreases to 3.36×10^{-10} kg^2 m^{-4} s^{-1} when the Al concentration is increased to 30 at. %, indicating that Ti-Al-Si-C-N coatings with larger Al concentrations have better oxidation resistance. X-ray diffraction, cross-sectional scanning electron microscopy, and x-ray photoelectron spectroscopy reveal a protective surface layer consisting of Al_2O_3, TiO_2, and SiO_2 that retards inward oxygen diffusion. A mechanism is proposed to elucidate the oxide formation. As a consequence of the good oxidation resistance, the Ti-Al-Si-C-N coatings have a large potential in high-speed dry cutting as well as other high temperature applications. [http://dx.doi.org/10.1116/1.4721376]

I. INTRODUCTION

Hard coatings are commonly used to enhance the surface wear resistance and oxidation resistance of mechanical parts. TiN, the first-generation hard coating, is still widely used in protective coatings; however, TiN hard coatings can be easily oxidized at temperatures greater than 500 °C and are thus not suitable for applications requiring a high operating temperature.[1] As a more advanced hard coating, TiAlN can better resist oxidation up to 800 °C (Refs. 2 and 3) and the incorporation of aluminum into TiN-based hard coatings can improve the oxidation resistance due to its excellent anti-oxidation properties.[4] Vaz *et al*. studied thermal oxidation of TiAlN coatings in air.[5,6] In their study, a bilayered structure consisting of a protective Al_2O_3 surface layer with a trace amount of Ti and an aluminum-depleted zone were formed between 750 °C and 900 °C. The oxidation rate was impacted by the Al_2O_3 layer and their results suggested that increasing the Al concentration in TiAlN coatings could reduce the oxygen diffusion rate through the mixed oxide (Al_2O_3 and TiO_2) and consequently boost the oxidation resistance.

TiAlN coatings have attracted much attention[7–9] and have been used in cutting applications at elevated temperatures,[10–13] but further improvements to the wear resistance by the addition of extra elements are in demand by the high-speed dry cutting industry. The addition of Si (the range of Si content is from 6–12 at. %) to TiAlN produces an amorphous Si_3N_4 phase surrounding the nanocrystalline (Ti, Al)N_x grains in the Ti-Al-Si-N coatings, and the nanocomposite structure of nc-(Ti, Al)N_x/a-Si_3N_4 enhances the coating hardness up to 50 GPa.[14,15] The super hardness of these nanocomposites stems from the crystalline and amorphous phases giving rise to high cohesive energy at the interface.[16–18] A higher content of Si (more than 20 at. %) in (Me, Si)N_x coatings increases oxidation resistance above 1000 °C, even up to 1500 °C; here Me = Zr, Ta, Ti, Mo, W, Al, etc.[19] This good oxidation resistance is attributed to the amorphous structure of coatings with a high Si content (more than 20 at. %).[20,21] However, the hardness of these coatings is low (about 20 GPa). Our previous study showed that incorporation of carbon into the nanocomposite Ti-Si-N coatings led to the formation of a graphitelike lubricious phase of amorphous carbon,[22] and the friction coefficients of the Ti-Si-C-N coatings with high carbon concentrations were lower at both room and elevated temperatures. The reason for the friction reduction is that the small TiC carbide or Ti(C, N) carbonitride grains disrupt the atomic bonding continuity in the amorphous carbon, thus weakening the structural integrity and facilitating the release of carbon from the coating due to graphitization.[23–25] Hence, both hardness enhancement and friction reduction can be accomplished by incorporating Si and C to wear-resistant TiAlN coatings. In this article, the Ti-Al-Si-C-N coatings need to have a hardness of nearly 40 GPa, so 10 at. % Si content is selected.

New quintuple hard coatings of Ti-Al-Si-C-N may exhibit both better oxidation resistance and wear resistance than traditional coatings. Indeed, Ti-Al-Si-C-N coatings have been found to possess better hardness and lower friction than conventional TiAlN coatings.[26] However, the oxidation resistance, which is crucial to applications requiring a high operating temperature, is not well understood for these new coatings. In this work, the oxidation resistance of Ti-Al-Si-C-N coatings with different Al concentrations and the associated mechanism are

[a]Author to whom correspondence should be addressed; electronic mail: slma@mail.xjtu.edu.cn

investigated systematically to elucidate the relationship between the temperature and surface composition, as well as microstructure.

II. EXPERIMENTAL DETAILS

A hybrid arc-enhanced magnetron sputtering (AEMS) system shown in Fig. 1 was used to produce the Ti-Al-Si-C-N coatings. The high plasma density produced by the titanium arc source enhanced adhesion between the coating and the substrate. In addition, three pairs of dual-magnetron targets including two Al targets, two C targets, and two Si targets were installed along the vacuum chamber wall. Two planar magnetrons for each pair were placed in the vacuum chamber with a rotating substrate holder in the center. A pulsed direct current power supply with 40 kHz pulse frequency was used on the substrate and three pulsed alternating current power supplies with 40 kHz pulse frequency were utilized on each pair of dual-magnetron targets to control the substrate bias voltage, substrate bias current, and target power. The substrate bias power supply was operated in the unipolar pulse mode and the pulse-on to pulse-off ratio was adjusted according to the processing requirements. The medium-frequency power supplies were operated in the constant current mode to control the magnetron targets.

Before deposition, the polished high-speed steel (HSS) substrates and Si wafers were cleaned ultrasonically in acetone and ethanol. After pumping down to a background pressure of 6.0×10^{-3} Pa by a turbo-molecular pump, the substrates were further cleaned in the glow discharge state by Ar ion bombardment at a bias voltage of -1000 V and duty ratio of 65% under an Ar atmosphere of 6 Pa for 20 min. The Ti-Al-Si-C-N coatings were synthesized using a bias voltage of -100 V, a substrate temperature of 200 °C, and pressure of 0.3 Pa in a mixture of Ar (flow rate of 30 sccm) and N_2 (flow rate of 28 sccm). The power applied to the C target (6 kW) and Si target (3 kW) as well as the current in the Ti arc ion target (60 A) were kept constant and only the Al target power was varied from 2.5–15 kW. The substrate-to-target distance was 120 mm. In order to enhance the adhesion strength between the coating and substrate, a TiN interfacial layer about 100 nm thick was first deposited with -500 V bias voltage onto the substrate. The as-deposited Ti-Al-Si-C-N coatings had a thickness of about 4.0 μm.

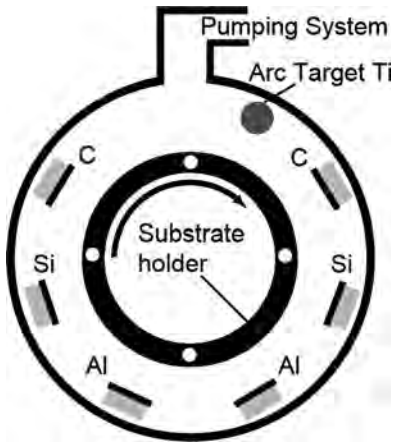

FIG. 1. Schematic diagram of the AEMS.

In order to assess the oxidation resistance of the Ti-Al-Si-C-N coatings, the samples were oxidized in air in the temperature range between 500 °C and 1000 °C for 1 h in a KSY conventional furnace. Afterwards, the samples were cooled naturally to room temperature inside the furnace and the weight change was measured using an electronic microbalance with a sensitivity of 10^{-5} g. The phase compositions of the coatings were investigated by x-ray diffraction (XRD) using Cu K_α radiation on a Rigaku D/max-3C diffractometer. The cross-sectional and surface morphologies of the coatings were examined by scanning electron microscopy (SEM, JSM 6700F). High-resolution transmission electron microscopy (HR-TEM, JEM 2100F), energy-dispersive spectrometry (EDS), and x-ray photoelectron spectroscopy (XPS, PHI 5802 spectroscopy) were performed to determine the structure and composition of the Ti-Al-Si-C-N coatings. The pass energy and the energy step size of XPS tests were 50 and 0.1 eV, respectively. Before conducting XPS, the samples were sputter-cleaned by Ar ions for 100 s to remove surface contamination. The HR-TEM tests were conducted at 200 keV. The hardness was determined by an HV-100 microhardness tester equipped with a Vickers diamond indenter at an applied load of 200 mN such that the penetration depth of the diamond indenter was below 0.28 μm (less than 1/10 of the coating thickness). The measurement error of the HV-100 micro-hardness tester was approximately 10%. The grain size of the Ti-Al-Si-C-N coatings was estimated by the Scherrer formula

$$R = 0.9\lambda/(B\cos\theta), \tag{1}$$

where R is the grain size, λ is the Cu K_α wavelength (0.15418 nm), θ is the Ti-Al-Si-C-N (200) peak position, and B is the full-width at half-maximum (FWHM) of the measured peak.

III. RESULTS AND DISCUSSION

A. Microstructure

Table I lists the compositions of the as-deposited Ti-Al-Si-C-N coatings with different power applied to the Al target (2.5–15 kW). In order to simplify the nomenclature, only the content of Al is marked. The Al content increases from 9–30

TABLE I. Compositions of Ti-Al-Si-C-N coatings and the power applied to the Al target.

Coatings	Ti (at. %)	Al (at. %)	Si (at. %)	C (at. %)	N (at. %)	Power of Al target (kW)
$TiAl_9SiCN$	19	9	10	22	40	2.5
$TiAl_{12}SiCN$	18	12	12	22	36	5.0
$TiAl_{17}SiCN$	15	17	11	17	41	8.0
$TiAl_{25}SiCN$	6	25	9	16	45	12.0
$TiAl_{30}SiCN$	5	30	9	17	39	15.0

at. % and the Ti content decreases from 19–5 at. % as the Al target power increases from 2.5–15 kW, whereas the Si, C, and N contents are around 10, 17, and 40 at. %, respectively.

Figure 2 depicts the XRD patterns of the Ti-Al-Si-C-N coatings with Al concentrations varying from 9–30 at. % and oxidized at different temperatures. As the oxidation temperature is increased from 500 °C to 1000 °C, the intensity of the peaks at 42.4° and 36° arising from the (Ti,Al)(C,N) nanocrystalline phases increase. However, the FWHM decreases, indicating that the crystalline size increases with higher oxidation temperature.

Because the Gibbs free energy (ΔG^o) of Al_2O_3 for oxide formation is the lowest among Al_2O_3, TiO_2, and SiO_2, Al_2O_3 is formed preferentially, especially in the coatings with the higher Al contents as shown in Fig. 2. As the formed layer retards further inward oxygen diffusion, formation of TiO_2 and SiO_2 becomes more difficult at the lower temperatures. However, the rutile TiO_2 phase (JCPDS 00-021-1276) and anatase TiO_2 (JCPDS 00-021-1272) phase can be identified at high oxidation temperatures. This evidence agrees well with previous results.[9] Rutile is the stable form of TiO_2, whereas anatase is a metastable form of TiO_2 which transforms into rutile at high temperatures. For the coating with 9 at. % Al, the intensity of Al_2O_3 is too low to be identified. Based on these results, it is concluded that the oxide coating consists of rutile TiO_2, anatase TiO_2, and α-Al_2O_3.

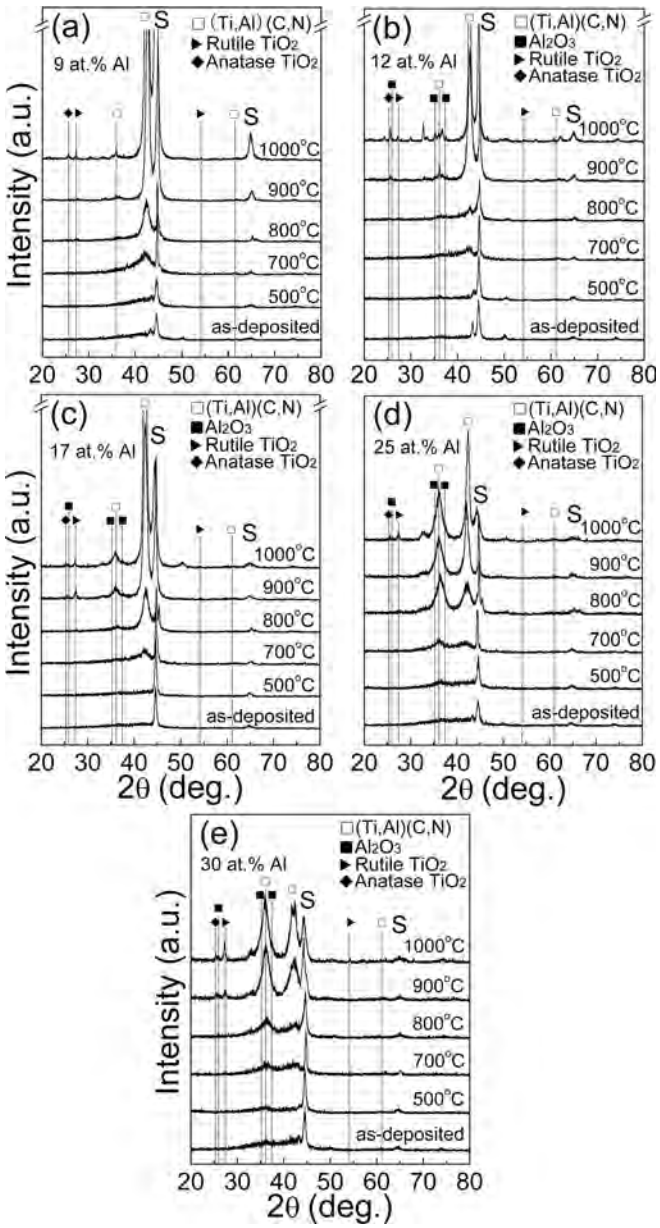

FIG. 2. XRD patterns of Ti-Al-Si-C-N coatings after oxidation: (a) 9 at. % Al, (b) 12 at. % Al, (c) 17 at. % Al, (d) 25 at. % Al, and (e) 30 at. % Al. S indicates the peak positions of the HSS substrate.

The cross-sectional SEM micrograph of the Ti-Al-Si-C-N coating with 25 at. % Al oxidized at different temperatures for 1 h is shown in Fig. 3. A surface oxide can be observed after oxidation between 500 °C and 1000 °C and the oxide thickness increases with oxidation temperature. When the oxidation temperature is between 500 °C and 900 °C, the oxide layer is relatively thin at less than 0.2 μm. However, after oxidation at 1000 °C, the oxide layer thickness increases significantly to about 2 μm. This is consistent with previous findings[6] that a surface Al_2O_3 layer forming during oxidation protects the underlying coating from further oxidation. Furthermore, because oxidation is a process of oxygen diffusion from the surface to the inner side, except for the oxide layer, the composition of the inner layer is identical to the as-deposited coating.

The XPS results in Fig. 4 reveal the presence of Ti-C, Ti-N, Al-N, and Si-N bonds in the as-deposited sample. After oxidation at 1000 °C, these chemical bonds are gradually converted into Ti-O, Al-O, and Si-O. The intensity of Al in Fig. 4(b) increases with temperature, suggesting that Al is transported to the surface during oxidation, forming an Al-rich surface layer which protects the substrate from further oxidation. These results are also consistent with previous findings.[4,5] The XRD results in Fig. 2 clearly show the TiO_2 and Al_2O_3 peaks, but no SiO_2 peak is visible. As reported in the literature,[4,9,27] the amorphous Si_3N_4 is converted to amorphous SiO_2 due to oxygen diffusion. Hence, it is concluded that the surface oxide consists of anatase and rutile TiO_2, α-Al_2O_3, and also amorphous SiO_2. The C1s and N1s spectra are shown in Figs. 4(e) and 4(f), respectively. As shown, C and N cannot be detected on the surface of coatings after oxidation at 800 °C and 700 °C, respectively.

The plan-view HR-TEM images of the Ti-Al-Si-C-N coating with 25 at. % Al oxidized at different temperatures are shown in Fig. 5, and the corresponding selected area electron diffraction (SAED) patterns are shown on the left corner of each image, respectively. According to the EDS results which are not shown in this article, the compositions of HR-TEM samples are identical to that of the as-deposited coating. The oxygen element was not found in the samples. The oxide layer might peel off when the HR-TEM sample was produced. It can be seen that although the grain size increases gradually with oxidation temperature, the nanocomposite structure nc-(Ti,Al)(C,N)/ a-Si_3N_4/a-C is quite stable. According to XRD and XPS results, Si displays only as amorphous Si_3N_4 in as-deposited coatings. Therefore, Si

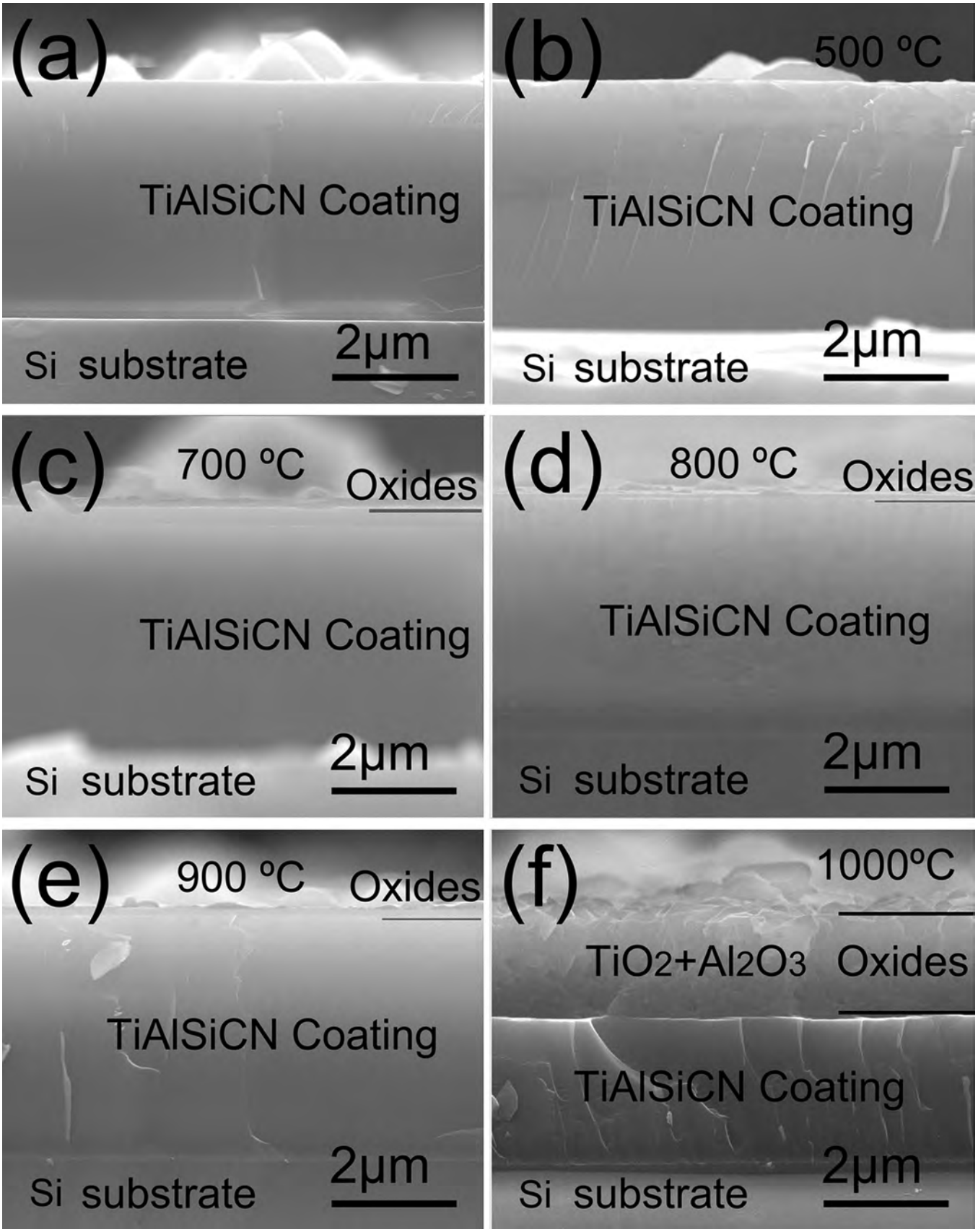

FIG. 3. Cross-sectional SEM micrographs of Ti-Al-Si-C-N coatings with 25 at. % Al: (a) As-deposited, (b) 500 °C, (c) 700 °C, (d) 800 °C, (e) 900 °C, and (f) 1000 °C.

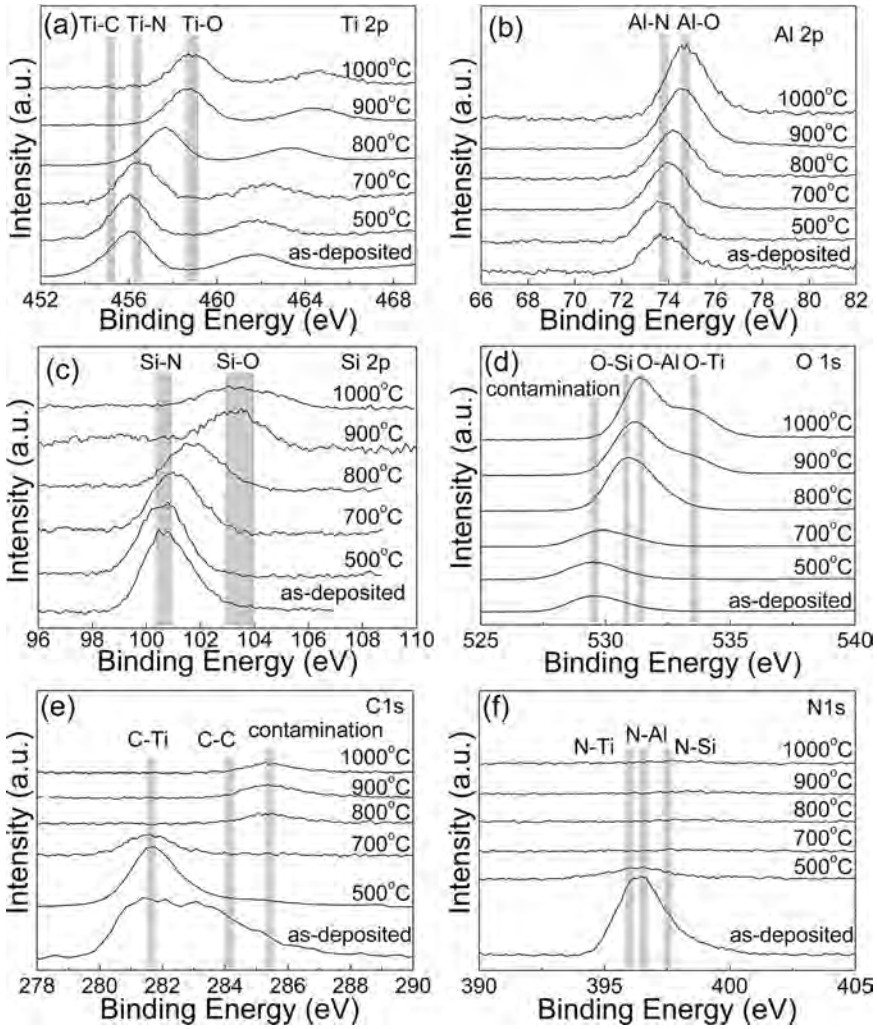

FIG. 4. XPS spectra of as-deposited and oxidized Ti-Al-Si-C-N coatings with 25 at. % Al: (a) Ti2p, (b) Al2p, (c) Si2p, (d) O1s, (e) C1s, and (f) N1s.

is not incorporated in the (Ti,Al)(C,N) crystalline phase. The SAED patterns indicate the existence of (Ti,Al)(C,N) crystalline phases with (111), (200), (220) crystalline orientations. The diffraction circles become more distinct with increasing oxidation temperature, implying refinement of the crystal structure for which grain growth will occur with increases in temperature and lead to a clearer SAED pattern.

Surface morphologies for the oxidized Ti-Al-Si-C-N samples with 9 and 30 at. % Al are presented in Figs. 6 and 7, respectively. The as-deposited coating is included for direct comparison. As shown in Fig. 6, the sample surface after oxidation at 500 °C–700 °C is smooth. After heat treatment at 800 °C, small crystallites emerge as shown in Fig. 6(d). When the temperature increases to 900 °C, even larger and denser crystallites are exhibited [Fig. 6(e)]. According to the XRD results in Fig. 2, oxide is present at this point [Fig. 6(e)]. At 1000 °C, the average crystallite size increases to more than 200 μm, implying significant oxidation [Fig. 6(f)]. In comparison, Fig. 7 shows that the 30 at. % Al samples after oxidation at 500 °C–900 °C still have smooth surfaces. At 1000 °C, a few small crystallites emerge on the surface as shown in Fig. 7(f). Comparing the images in Figs. 6 and 7, it can be concluded that the oxidation resistance increases as the Al content increases.

B. Microhardness

Figure 8 shows the effect of the oxidation temperature on the microhardness and grain size of the Ti-Al-Si-C-N coatings with different Al contents. The grain size is estimated by the Sherrer formula using the XRD data in Fig. 2. The hardness and grain size of the coatings with 9 and 12 at. % Al are almost the same after treatment at 800 °C, but further increases in the oxidation temperature reduce the coating hardness and increase the grain size. When the Al concentration is increased to 17 and 25 at. %, the hardness and grain size are maintained up to 900 °C. However, after oxidation at 1000 °C, the hardness decreases to about 20 GPa. For the coating with 30 at. % Al, the hardness is maintained up to 1000 °C. Although the grain size increases slightly, it is still less than 10 nm. It is noted that the hardness increases from 32–36 GPa when the oxidation temperature is increased from 500 °C–800 °C. This phenomenon may be due to refinement of the crystallites at high temperatures.

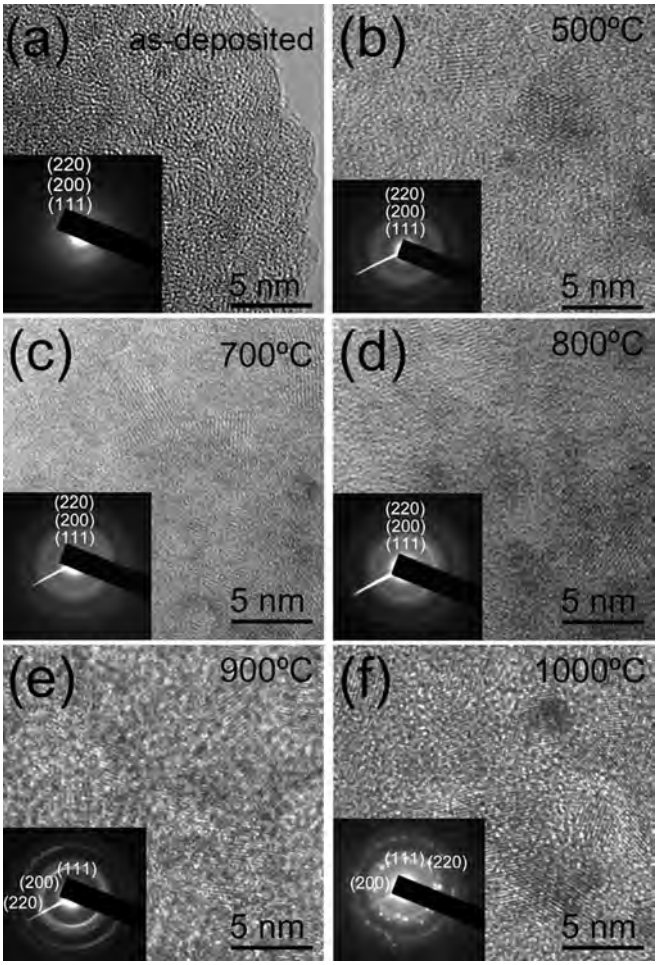

FIG. 5. Plan-view HR-TEM images and SAED patterns of Ti-Al-Si-C-N coatings with 25 at. % Al : (a) As-deposited, (b) 500 °C, (c) 700 °C, (d) 800 °C, (e) 900 °C, and (f) 1000 °C.

C. Oxidation kinetics

In order to evaluate the oxidation kinetics, weight change was measured after oxidation at different temperatures. Ti-Al-Si-C-N coatings with HSS substrates were used. Figure 9 shows the weight change per unit area ($\Delta W/A$) as a function of oxidation temperature from 500 °C–1000 °C. No weight change can be observed for the coating with 9 at. % Al at temperatures less than 800 °C. However, an obvious mass gain is observed after oxidation at 900 °C, indicating the onset of substantial oxidation around this temperature. The results obtained for the sample with 12 at. % Al are very similar to those for the 9 at. % Al coating. No obvious mass change can be detected from the samples with 17 and 25 at. % Al below 900 °C, but at 1000 °C, oxidation can be observed. In comparison, very little mass change can be detected for the coating with 30 at. % Al up to 1000 °C, indicating that this coating has the best oxidation resistance. The relationship between $(\Delta W/A)^2$ and oxidation time is approximately linear[4–6] and the oxidation kinetics can be described by the following parabolic relationship:

$$(\Delta W/A)^2 = K_p \cdot t, \tag{2}$$

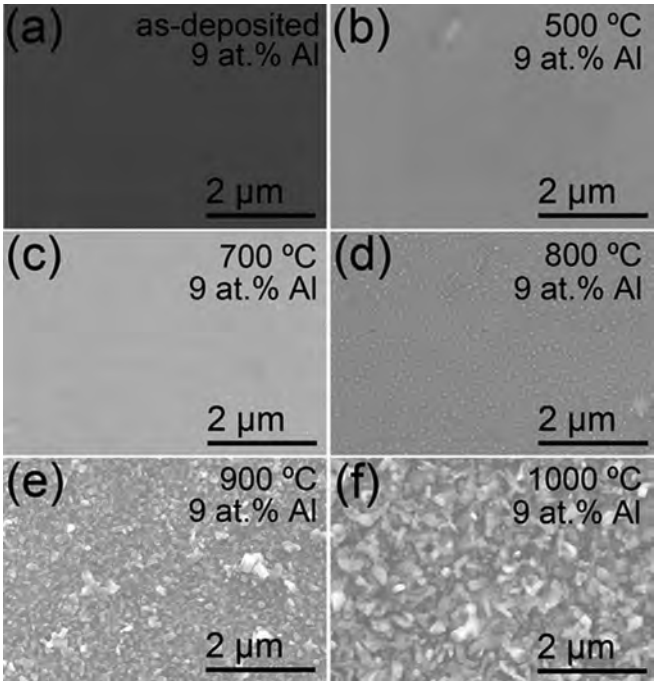

FIG. 6. Plan-view SEM micrographs of Ti-Al-Si-C-N coatings with 9 at. % Al: (a) As-deposited, (b) 500 °C, (c) 700 °C, (d) 800 °C, (e) 900 °C, and (f) 1000 °C.

where K_p is a parabolic oxidation rate constant and t is the oxidation time. K_p can be calculated using the results in Fig. 9, and Fig. 10 shows the K_p values of the Ti-Al-Si-C-N coatings oxidized between 800 °C and 1000 °C. The K_p value of the Ti-Al-Si-C-N coating increases with oxidation temperature, indicating that the oxidation rate also increases. In

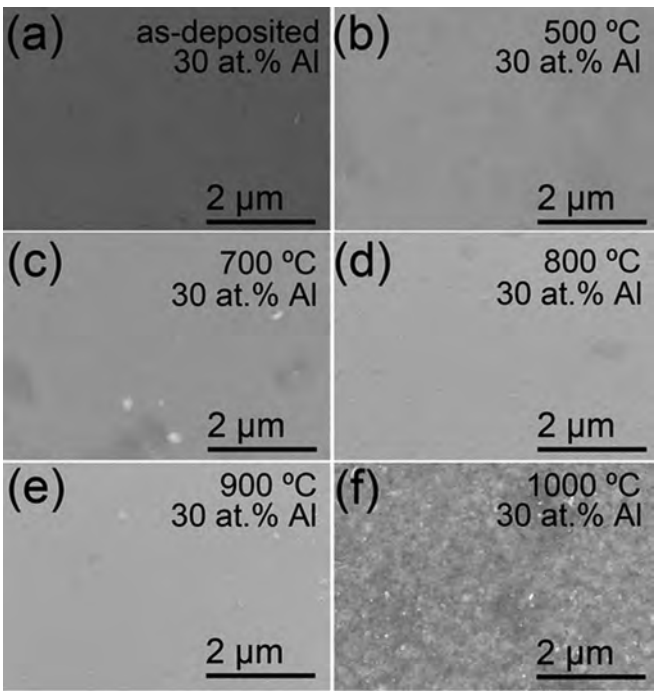

FIG. 7. Plan-view SEM micrographs of Ti-Al-Si-C-N coatings with 30 at. % Al: (a) As-deposited, (b) 500 °C, (c) 700 °C, (d) 800 °C, (e) 900 °C, and (f) 1000 °C.

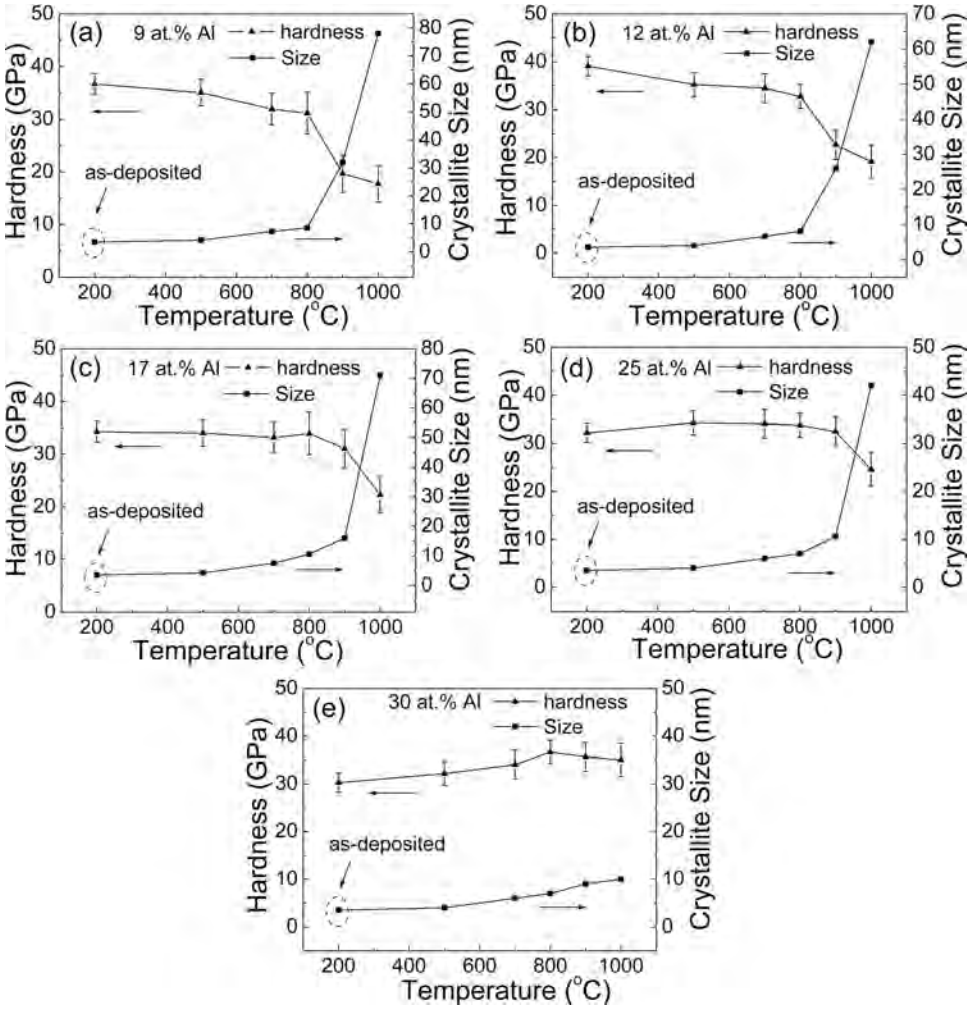

FIG. 8. Microhardness and crystallite size of Ti-Al-Si-C-N coatings after oxidization: (a) 9 at. % Al, (b) 12 at. % Al, (c) 17 at. % Al, (d) 25 at. % Al, and (e) 30 at. % Al.

addition, at the same oxidation temperature, K_p decreases as the Al content increases. Hence, better oxidation resistance is achieved from the samples with larger Al content. Because the K_p values are different, there are differences in surface crystallization shown in Figs. 6 and 7. The overall parabolic rate constant K_p and oxidation temperature can be described using the Arrhenius relationship[28,29]

$$K_p = A\exp(-E/R\cdot T), \tag{3}$$

where A is the pre-exponential factor, E is the apparent activation energy, T is the absolute temperature, and R is the universal gas constant (8.3145 J/mol·k). Equation (3) can be converted into the following form:

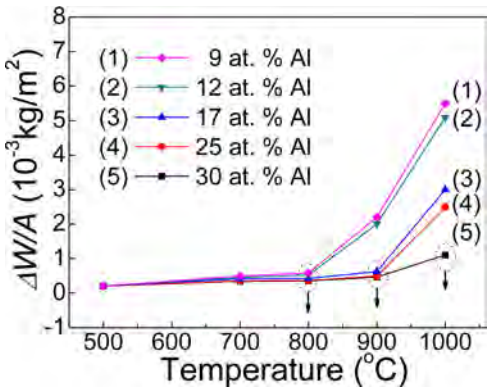

FIG. 9. (Color online) Mass change measured from the Ti-Al-Si-C-N coatings with different Al contents after oxidation.

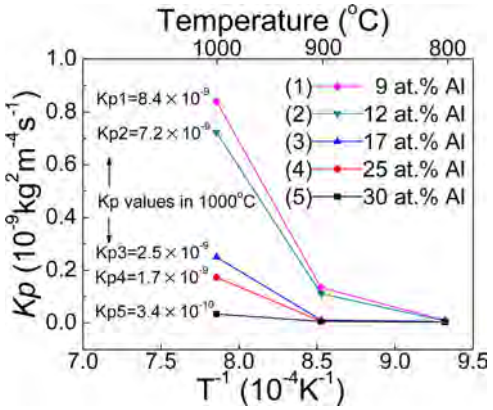

FIG. 10. (Color online) K_p values of the Ti-Al-Si-C-N coatings oxidized at temperatures between 800 °C and 1000 °C. The K_p values of the samples with different Al concentrations oxidized at 1000 °C are shown on the left.

$$\mathrm{Ln}\,K_p = \mathrm{Ln}\,A - (E/R)(1/T). \quad (4)$$

Figure 11 shows the temperature dependence of $\mathrm{Ln}K_p$ for the Ti-Al-Si-C-N coatings in the temperature range of 800 °C–1000 °C. According to Eq. (4), the E value is calculated by the slope of the linear fit in Fig. 11. E values of Ti-Al-Si-C-N coatings are shown on the right side in Fig. 11, indicating that E decreases with increasing Al content. The E value calculated from the Ti-Al-Si-C-N coating with 30 at. % Al is 127 kJ/mol. It is much smaller than the others and reflects the best oxidation resistance, in accordance with previous reports.[4–6] E represents the energy difference between the initial state and intermediate state.[29] Because it is easier to form the Al_2O_3 layer with higher Al content, the E value would decrease with increasing Al content, and the coating would show better oxidation resistance with higher Al content.

According to the discussion above and the results in Fig. 3, the mechanism of the oxidation resistance can be described as follows: when the oxidation temperature is below 900 °C, oxidation is not extensive and a very thin surface oxide layer is formed. Based on the previous discussion, it can be concluded that this oxide layer can effectively reduce the diffusion rate of oxygen and protect the underlying coating from further oxidation. A higher Al content decreases the parabolic oxidation rate constant K_p, as shown in Fig. 10, and consequently increases the oxidation resistance. An Al-rich surface layer is formed after oxidation and the oxidation rate is governed by the Al_2O_3 layer and intermediate (Ti, Al)O_x layer.[5] As the Al content is increased, the oxygen diffusion rate through the mixed oxide layer decreases and the overall oxidation resistance is improved. It should be noted that in the absence of this Al_2O_3 protective layer, the oxidation resistance will be compromised.

As discussed previously, the surface oxide consists of anatase and rutile TiO_2, α-Al_2O_3, and amorphous SiO_2. Anatase TiO_2 is a metastable form of TiO_2 and will be converted into rutile at high temperatures. It has been reported that oxidation at temperatures exceeding 600 °C cannot form anatase TiO_2 on metallic Ti.[30] However, in this study anatase TiO_2 is detected at temperatures above 800 °C. In fact, similar results have been obtained indicating that silicon stabilizes the anatase phase.[9,31] Since the amorphous Si_3N_4 and SiO_2 surround the nanocrystallites, the growth of titanium oxide grains is inhibited and anatase TiO_2 can exist in coatings. The Gibbs free energies (ΔG^o) pertaining to the formation of Al_2O_3, TiO_2, and SiO_2 are −1336, −753, and −725 kJ/mol, respectively.[32] Therefore, Al_2O_3 is formed preferentially and retards further oxygen diffusion. In comparison, TiO_2 and SiO_2 are harder to form and SiO_2 should be converted by Si_3N_4 *in situ*. The amorphous SiO_2 may block metal out-diffusion and oxygen in-diffusion, giving rise to improved oxidation resistance.[9] Nitrogen and carbon in the oxide layer are released to the environment through the oxide layer during oxidation. When the oxidation temperature is increased to 1000 °C, the oxide layer is thicker than that at 900 °C due to the larger K_p at 1000 °C. In addition, the crystallites in coatings grow to a relatively large size.

Figure 8(d) shows that the hardness and crystallite size of the Ti-Al-Si-C-N coating with 25 at. % Al are nearly constant up to 900 °C. However, at 1000 °C, the hardness observably decreases and the crystallite size increases to about 42 nm. According to the results above, the nanocomposite structure is stable at temperatures under 900 °C and so the hardness is maintained. However, at 1000 °C, the nanocomposite structure is destroyed due to substantial growth of the crystallites which would diminish the hardness. Another reason for the decreased hardness is the formation of a surface oxide layer, which has a lower hardness than the as-deposited coatings.[20]

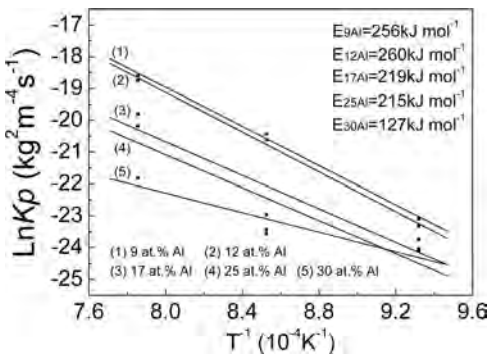

FIG. 11. Temperature dependence of $\mathrm{Ln}K_p$ for the oxidation of the Ti-Al-Si-C-N coatings with the calculated apparent activation energy E values showing on the right corner.

IV. CONCLUSION

The oxidation behavior of Ti-Al-Si-C-N coatings with different Al content was studied at varying temperatures. The Ti-Al-Si-C-N coating with 30 at. % Al content shows maximal oxidation resistance up to about 1000 °C. The parabolic oxidation rate constant K_p and apparent activation energy E decrease to 3.36×10^{-10} kg^2 m^{-4} s^{-1} and 127 kJ/mol, respectively, at 1000 °C as the Al content is increased to 30 at. %, suggesting improved oxidation resistance for samples with high Al content. The enhancement arises from the formation of a surface layer consisting of anatase TiO_2, rutile TiO_2, α-Al_2O_3, and amorphous SiO_2, protecting the underlying coating from further oxidation. The microhardness diminishes with increased oxidation temperature caused by the growth of crystallites and the formation of a surface oxide layer at higher oxidation temperatures, which has a lower hardness than the as-deposited coatings. The Ti-Al-Si-C-N coating with 30 at. % Al retains a high hardness of around 35 GPa even up to 1000 °C. With such excellent oxidation resistance, Ti-Al-Si-C-N coatings have great potential for high-speed dry cutting and other high temperature applications. Considering that the oxidation resistance of hard coatings could be further increased with higher Si content (more than 20 at. %), this will be the subject of our next investigation.

ACKNOWLEDGMENTS

This work was supported by the International Science and Technology Cooperation Program of China (No.

2008DFA51470), City University of Hong Kong Applied Research Grant No. 9667038, and Hong Kong Research Grants Council (RGC) General Research Funds (GRF) No. CityU 112510.

[1]C. W. Kim and K. H. Kim, Thin Solid Films **307**, 113 (1997).
[2]K. S. Lee, S. M. Seo, and K. A. Lee, Scr. Mater. **52**, 445 (2005).
[3]S. Seal, A. Kale, K. B. Sundaram, and D. Jimenez, J. Vac. Sci. Technol. A. **18**, 1571 (2000).
[4]L. Rebouta, F. Vaz, M. Andritschky, and M. F. Silva, Surf. Coat. Technol. **76–77**, 70 (1995).
[5]F. Vaz, L. Rebouta, M. Andritschky, M. F. Silva, and J. C. Soares, J. Eur. Ceram. Soc. **17**, 1971 (1997).
[6]M. Andritschky, F. Vaz, L. Rebouta, M. F. Silva, and J. C. Soares, Surf. Coat. Technol. **98**, 912 (1998).
[7]C. Rebholz, A. Leyland, A. Matthews, C. Charitidis, S. Logothetidis, and D. Schneider, Thin Solid Films **514**, 81 (2006).
[8]R. Rachbauer, E. Stergar, S. Massl, M. Mosera, and P. H. Mayrhofera, Scr. Mater. **61**, 725 (2009).
[9]M. Pfeiler, J. Zechner, M. Penoy, C. Michotte, C. Mitterer, and M. Kathrein, Surf. Coat. Technol. **203**, 3104 (2009).
[10]Z. Zhou, W. M. Rainforth, Q. Luo, P. E. Hovsepian, J. J. Ojeda, and M. E. Romero-Gonzalez, Acta Mater. **58**, 2912 (2010).
[11]W. Grzesik, Z. Zalisz, S. Krol, and P. Nieslony, Wear **261**, 1191 (2006).
[12]S. Veprek and M. Jilek, Vacuum **67**, 443 (2002).
[13]O. Knotek, M. Bohmer, and T. Leyendecker, J. Vac. Sci. Technol. A. **4**, 2695 (1986).
[14]S. Carvalho *et al*., Surf. Coat. Technol. **177–178**, 369 (2004).
[15]S. Carvalho, E. Ribeiro, L. Rebouta, C. Tavares, J. P. Mendonca, A. Caetano-Monteiro, N. Carvalho, J. Hosson, and A. Cavaleiro, Surf. Coat. Technol. **177–178**, 459 (2004).
[16]S. Carvalho, L. Rebouta, A. Cavaleiro, L. A. Rocha, J. Gomes, and E. Alves, Thin Solid Films **398–399**, 391 (2001).
[17]S. Q. Hao, B. Delley, S. Veprek, and C. Stampfl, Phys. Rev. Lett. **97**, 086102 (2006).
[18]S. Veprek, M. Haussmann, S. Reiprich, S. Z. Li, and J. Dian, Surf. Coat. Technol. **86–87**, 394 (1996).
[19]J. Musil, J. Vlcek, and P. Zeman, Adv. Appl. Ceram. **107**, 148 (2008).
[20]J. Musil, M. Sasek, P. Zeman, R. Cerstvy, D. Herman, J. G. Han, and V. Satava, Surf. Coat. Technol. **202**, 3485 (2008).
[21]J. Musil, V. Satava, P. Zeman, and R. Cerstvy, Surf. Coat. Technol. **203**, 1502 (2009).
[22]S. L. Ma, D. Y. Ma, Y. Guo, B. Xu, G. Z. Wu, K. W. Xu, and P. K. Chu, Acta Mater. **55**, 6350 (2007).
[23]N. Daniel, S. Fredrik, W. Urban, and H. Sture, Wear **254**, 1084 (2003).
[24]S. Imamura, H. Fukui, A. Shibata, N. Omori, and M. Setoyama, Surf. Coat. Technol. **202**, 820 (2007).
[25]H. Xu, X. Nie, and R. Wei, Surf. Coat. Technol. **201**, 4236 (2006).
[26]G. Z. Wu, S. T. Liu, S. L. Ma, K. W. Xu, V. Ji, and P. K. Chu, J. ASTM Int. **8**, 2 (2011).
[27]Y. Y. Chang, C. P. Chang, D. Y. Wang, S. M. Yang, and W. T. Wu, J. Alloy. Compd. **461**, 336 (2008).
[28]Z. J. Lin, M. S. Li, J. Y. Wang, and Y. C. Zhou, Acta Mater. **55**, 6182 (2007).
[29]M. Schwaab and J. C. Pinto, Chem. Eng. Sci. **62**, 2750 (2007).
[30]K. S. Lee and I. S. Park, Scr. Mater. **48**, 659 (2003).
[31]D. Pilloud, J. F. Pierson, M. Lucas, and A. Cavaleiro, Surf. Coat. Technol. **202**, 2413 (2008).
[32]Y. Y. Chang and C. Y. Hsiao, Surf. Coat. Technol. **204**, 992 (2009).